Investigation of the self-sealing of Opalinus Clay from the lower sandy facies of Mont Terri site by mock-up tests with highly saline and alkaline solutions

Yara Barakat, Nadia Mokni, Yu-Jun Cui, Pierre Delage, Frederic Bernier

Canadian Geotechnical Journal

Review

Investigation of the self-sealing of Opalinus Clay from the lower sandy facies of Mont Terri site by mock-up tests with highly saline and alkaline solutions

Yara Barakat[a,b], **Nadia Mokni**[a], **Yu-Jun Cui**[b], **Pierre Delage**[b], **and Frederic Bernier**[c]

[a]Institut de Radioprotection et de Sûreté Nucléaire (IRSN), PSE-ENV/SEDRE/LETIS, Fontenay-aux-Roses 92260, France; [b]Laboratoire Navier/CERMES, Ecole des Ponts ParisTech, Marne la Vallée, France; [c]Agence Fédérale de Contrôle Nucléaire (AFCN), Bruxelles, Belgium

Corresponding author: **Nadia Mokni** (email: nadia.mokni@irsn.fr)

Abstract

Three small-scale mock-up tests were carried out on artificially fractured Opalinus Clay samples from the lower sandy facies of Mont Terri site: the first with the synthetic water of neutral pH and at an osmotic suction of 1 MPa, the second with a highly $NaNO_3$ saline solution with a neutral pH and at osmotic suction of 34 MPa, and the third with a hyperalkaline solution at pH = 13.5 and at osmotic suction of 1.16 MPa. The radial swelling pressure was monitored using a total pressure sensor along with the fracture opening using a displacement transducer. The tests ran for over 290 days. After that, the three tests were dismantled. A detailed petrophysical characterization of 45 subsamples was conducted, and the pore size distribution was determined at different positions. X-ray diffractometry measurements were also conducted to identify any mineralogical changes. Results show that, in the case of the synthetic water and the alkaline solution, the friction forces exerted by the lid and the base on the sample were significant and probably hampered the self-sealing of the fracture. Saline solutions affect the self-sealing process of claystones. Indeed, even though increasing the salinity caused the contraction of the diffuse double layer and generated additional fractures within the sample, which increased the permeability and thus accelerated the hydration process, a complete self-sealing of the fracture opening was not observed.

Key words: self-sealing, salinity, alkalinity, Opalinus Clay, swelling, mineralogy, pore size distribution

1. Introduction

In Switzerland, the Opalinus Clay is considered as potential host rock for deep geological radioactive waste disposal (Andra 1999, 2005; Nagra 2002). A Damaged Zone can be created in the host rock during Excavation (EDZ) (e.g., Zhang 2013). This partially saturated EDZ is expected to be sealed with underground water seepage (Zhang 2011; Menaceur et al. 2016; Zhang 2016). However, due to the degradation of concrete resulting in the release of alkaline plumes, the pH of the underground water, initially at 7.5 (Pearson et al. 2003; Gaucher and Blanc 2006), is expected to increase up to 13.5 (Taylor 1987; Ye et al. 2014). Furthermore, the osmotic suction (π) of the groundwater, initially at 1 MPa in Opalinus Clay (Ferrari et al. 2014; Gonzalez-Blanco 2017), is expected to increase significantly (Thyagaraj and Rao 2013; He et al. 2016) due to the release of saline plumes from the bituminized saline wastes. These chemical perturbations will certainly affect the hydromechanical properties and the self-sealing behavior of the host rock. While the self-sealing behaviors of Opalinus Clay and Callovo-Oxfordian claystones have been investigated in several studies (Dixon et al. 2002; Davy et al. 2007; Zhang and Rothfuchs 2008; Zhang 2011, 2013; Monfared et al. 2014; Menaceur et al. 2016) using triaxial cells and synthetic water with the chemical composition similar to the site pore water, the impact of salinity and alkalinity was poorly addressed (e.g., Geet et al. 2008). Indeed, even though Geet et al. (2008) investigated the effect of salinity and alkalinity on the self-sealing capacity of argillaceous rocks, a further investigation is still needed in this field. In this study, a new experimental device allowing the monitoring of the self-sealing process of the Opalinus Clay using multiple sensors was used, and the impact of both saline and alkaline solutions on self-sealing was investigated. Indeed, after exposing three artificially fractured samples for over 290 days to either synthetic water (π = 1 MPa; pH = 7.5), a highly saline solution (π = 34 MPa; pH = 7.5) or a hyperalkaline solution (π = 1.16 MPa; pH = 13.5), a detailed petrophysical characterization of 45 subsamples was conducted. Also, the pore size distribution was determined for different positions using both mercury intrusion porosimetry (MIP) and nitrogen adsorption–desorption techniques. X-ray diffractometry measurements were also performed. These characterizations are the first to be conducted on exposed Opalinus Clay samples and will allow on the one hand, the improvement of the new

Table 1. Mineralogical composition (wt.%) of the Opalinus Clay from the lower sandy facies of Mont Terri site, Switzerland.

Mineral	Lerouge (2014)	Ould Bouya (2014)
Clay fraction	**38%**	**52%**
Illite	14%	35%
Chlorite	1%	7%
Kaolinite	9%	9%
I/R (Type R1)	14%	–
Carbonate fraction	**20%**	**10%**
Calcite	8%	7%
Dolomite	12%	3%
Silty fraction	**38%**	**37%**
Feldspars	6%	3%
Quartz	32%	34%
Pyrite	**4%**	**1%**
Total	**100%**	**100%**

experimental device and on the other hand, the better understanding of the impact of salinity and alkalinity on the self-sealing behavior of natural claystones.

2. Materials

2.1. Claystone studied

The material studied is the Opalinus Clay from the lower sandy facies (LSF) of the Mont Terri URL in Switzerland. The samples were collected from a 0.35 m core from BSW-B26 borehole drilled in February 2020 in the LSF in the vertical direction, thus with an angle of 43° to the bedding plane.

The mineralogical composition % of the LSF Opalinus Clay identified by X-ray diffraction (XRD) on bulk rock samples is shown in Table 1. According to both studies (Lerouge 2014; Ould Bouya 2014), the silty fraction is dominated by quartz. However, the carbonate fraction varies between 10% and 20% and the clay fraction varies between 38% and 52%. Indeed, this is due to the heterogeneity of the LSF in terms of mineralogy as identified by Kneuker and Furche (2021). This is also consistent with the different subfacies constituting the LSF addressed in Lauper et al. (2018). It has to be noted that the smectite is present in the form of interstratified illite/smectite type R1 (i.e., 80% illite and 20% smectite) and that according to Lerouge (2014), the clay and quartz fractions are both equal to 38%.

The basic properties of the LSF Opalinus Clay samples investigated in this study are listed in Table 2. Samples, taken from different locations of the studied core, were investigated to determine the initial state. The water content, determined by oven-drying at 105 °C for 24 h, ranged between 0.89% and 1.66%. Measurements of sample total volume, mass, and water content allowed to calculate the bulk saturated density, the bulk dry density, the void ratio, and the degree of saturation. The sample total volume was determined based on the Archimedes' principle after immersion into a dearomatized hydrocarbon, following the experimental protocol proposed by Monnier et al. (1973) and adapted to Mont Terri claystone (Matray et al. 2007; Matray and Möri 2012). The soil density was calculated from the dry mass and soil solid volume that was measured using the helium pycnometer based on the volume–pressure relationship of Boyle's Law. The bulk saturated density, the bulk dry density, and the soil solid density are 2.28−2.45, 2.26−2.43, and 2.68−2.72 Mg/m^3, respectively. The ranges of both the bulk saturated density and the bulk dry density are lower than the values reported by Yu (2017) for the LSF. The initial low range of water content (w = 0.89%–1.66%) and degree of saturation (S_r = 11.93%–34.42%) of the samples used in this study are due to the poor storage conditions. Indeed, the cores were not properly sealed upon reception. Consequently, the bulk saturated density is lower than that expected in the LSF (2.52–2.55 Mg/m^3).

2.2. Hydration solutions

Three solutions were used to hydrate the samples, as indicated in Table 3. The first one is the synthetic water, with a chemical composition similar to that of the pore water in the LSF (Table 4) (Pearson et al. 2003; Yu 2017). It has a neutral pH of 7.5 and an osmotic suction of π = 1 MPa. The osmotic suction and pH of the solution were measured with a WP4 Dewpoint PotentiaMeter (Decagon Devices, Inc.) and with a conventional pH meter, respectively. Before using it, the WP4 was calibrated using a buffer KCL solution. The pH meter is a WTW model Multi 3420, with a probe model from SI Analytics GmbH with a measuring range from 1 to 14. Before use, the pH meter was calibrated using four standard buffer solutions at 4, 6.8, 9.1, and 12, respectively.

Since the pH of the groundwater is expected to vary due to concrete degradation during the operational phase of the repository, a second hyper alkaline solution of pH = 13.5 was also used, with the same chemical components and pH as the concrete pore water (Table 5). The osmotic suction of the hyperalkaline solution is π = 1.16 MPa, almost like the osmotic suction of the synthetic water. Furthermore, since the groundwater salinity is expected to increase, a third sodium nitrate solution of π = 34 MPa was also used. Indeed, the bituminized saline wastes are expected to release sodium nitrate plumes. The equation that relates the concentration of sodium nitrate with the osmotic suction and is used to prepare the saline solution is as follows (e.g., Mokni 2011):

$$\pi = -\frac{RT\rho_l}{M_w}\ln\left[1-\left(\frac{cM_s}{\rho_l}\right)^2\right] \quad (1)$$

where R = 8.31 J/(mol K) is the gas constant, T = 293 K is the temperature, M_w = 18.016 kg/kmol is the molar mass of water, M_s = 85 kg/kmol is the molar mass of the sodium nitrate, ρ_l (kg/m^3) is the liquid density, and c (mol/L) is the concentration.

The saline solution has a pH of 7, similar to that of the synthetic water; therefore, no contribution from the pH should be considered in the case of the $NaNO_3$ solution.

Table 2. Basic properties of the Opalinus Clay from the lower sandy facies of Mont Terri site, Switzerland.

Properties	Values measured in this study	Values from the literature for Opalinus Clay	References	Values from the literature for Opalinus Clay from the lower sandy facies	References
Bulk saturated density (Mg/m^3)	2.28–2.45	2.45–2.62	Yu (2017)	2.52–2.55	Yu (2017)
		2.40–2.53	Bossart (2011)		
Bulk dry density (Mg/m^3)	2.26–2.43	2.31–2.48	Yu (2017)	2.42–2.46	Yu (2017)
		2.28–2.32	Bossart (2011)		
Soil density (Mg/m^3)	2.68–2.72	2.67–2.91	Yu (2017)	2.70–2.71	Yu (2017)
		2.7–2.77	Bossart (2011)		
Total porosity (%)	9.92–16.86	9.1–21.5	Yu (2017)	9.1–10.3	Yu (2017)
		14–24.7	Bossart (2011)		
Water content (%)	0.89–1.66	3.22–6.4	Yu (2017)	3.22–3.6	Yu (2017)
		5.3–9.8	Bossart (2011)		
Saturation degree (%)	11.93–34.42	47–98.2	Yu (2017)	83.8–86.4	Yu (2017)
Void ratio	0.11–0.2	–			
pH of pore water	–	7.3–7.96	Pearson et al. (2003); Bossart and Thurry (2008)		
Cation exchange capacity (meq/100 g)	–	9.44–13.35	Pearson et al. (2003); Bossart and Thurry (2008)	9.34	Yu (2017)
Main exchanged cation (meq/100 g)	–	Ca^{2+} (1.54–3.75), Sr^{2+} (0.01–0.25), Na^{+} (0.03–2.12), K^{+} (0.03–1.39), Mg^{2+} (0.24–1.23)	Yu (2017)	Ca^{2+} (3.53), Sr^{2+} (0.14), Na^{+} (1.52), K^{+} (1.25), Mg^{2+} (0.95)	Yu (2017)

Table 3. Hydration solutions used in this study.

Solution	Type	Osmotic suction	Solute mass fraction	pH
1	Synthetic solution	1 MPa	–	7.5
2	Saline solution—$NaNO_3$	34 MPa	0.45	7
3	Alkaline solution—NaOH − KOH − Ca $(OH)_2$	1.16 MPa	–	13.5

Table 4. Chemical composition of the synthetic water of the Opalinus Clay from the lower sandy facies of Mont Terri site, Switzerland (Yu 2017).

Compound	Concentration (mol/L)
NaCl	1.38×10^{-1}
KCl	4.04×10^{-2}
$CaCl_2$	1.3×10^{-2}
$MgCl_2$	1.3×10^{-2}
$NaHCO_3$	1.94×10^{-3}
$Na_2S_2O_3$	8.84×10^{-3}

Table 5. Chemical composition of the concrete pore water (Lalan 2016).

Compound	Concentration (mol/L)
NaOH	5×10^{-2}
KOH	2.7×10^{-1}
$Ca(OH)_2$	6×10^{-4}

3. Methods

3.1. Sample preparation

In this study, the self-sealing experiments were conducted on artificially fractured LSF Opalinus Clay samples with a controlled fracture opening. The samples were prepared from the initial core by overcoring with a 5 cm diameter diamond corer and by cutting with a diamond wire saw to reach the desired thickness of 2 cm (Fig. 1*a*). To artificially generate the fracture, the samples were cut into two halves by means of the diamond wire saw (Fig. 1*b*). To achieve the desired fracture opening of 1 mm, the two half-samples were polished with an abrasive paper. The final fracture opening varies between 1 and 1.5 mm. Two notches were engraved in the two half-samples to ensure a proper installation of the blades of the displacement transducer (Fig. 1*c*).

3.2. Experimental setup and tests

The experimental setup for the self-sealing experiments is shown in Fig. 2. It consists of a constant volume cylindrical cell with three sensors: a total pressure sensor monitoring the total radial swelling pressure (Fig. 2*a*), a mini-

Fig. 1. Sample preparation. (*a*) Full sample of 5 cm in diameter and 2 cm in thickness. (*b*) Artificially fracturing the sample with a wire saw. (*c*) Half-sample with notch.

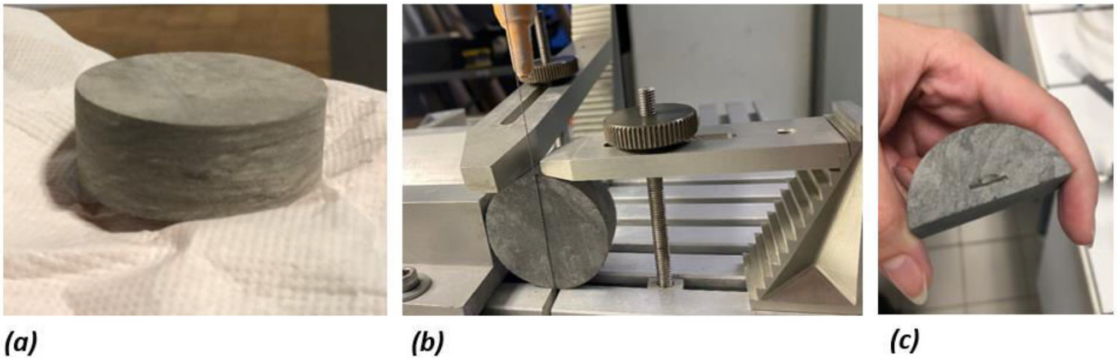

Fig. 2. (*a*) ED view. (*b*) Cross-section A–A.

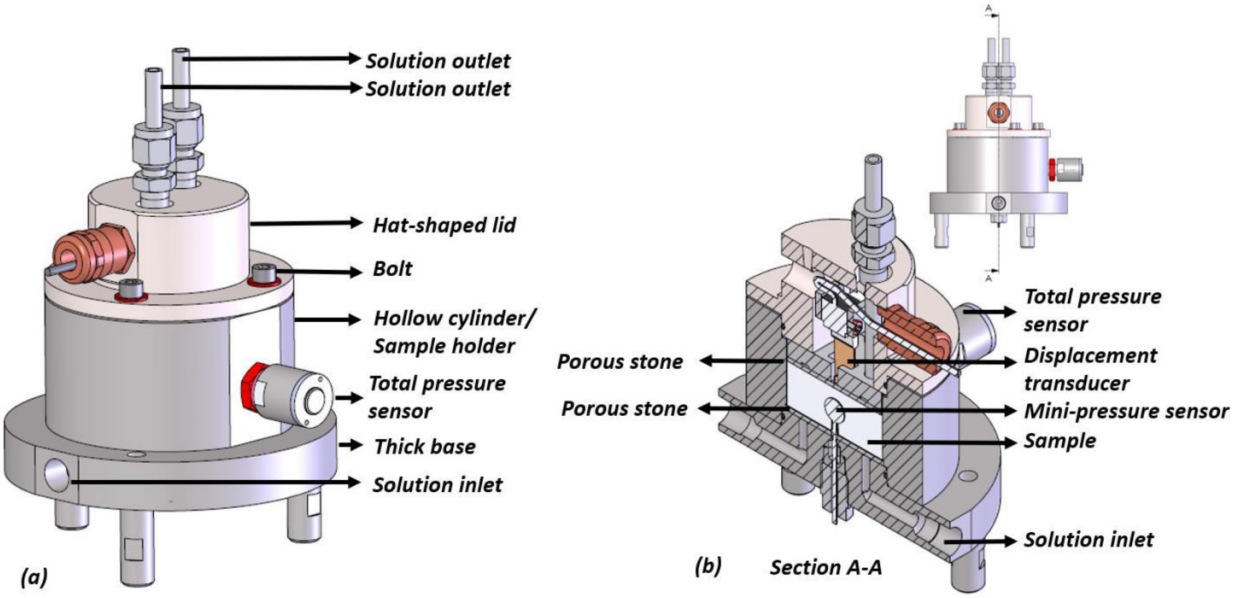

pressure sensor inserted within the artificially created fracture, to measure pressure changes during the sealing process, and a displacement transducer tracking the closure of the diametric fracture (Fig. 2*b*). The total pressure sensor is a Kyowa pressure sensor PS-10KD/PS-50KD M2. The mini-pressure sensor inserted within the fracture is an ultrathin Kyowa pressure sensor PS-10KC. Finally, the displacement transducer is a Kyowa clip-type displacement transducer DTC-A-2. Fluid infiltration is carried out from the cell bottom (Fig. 2*b*). The cell is equipped with outlets to allow air escape (Fig. 2*a*). Once the fluid comes out of the top, the outlets are closed. A data logger is used to automatically record the radial swelling pressure, the pressure within the fracture, and the displacement.

The three tests considered in this study are presented in Table 6. In tests 2 and 3, no mini-pressure sensor was installed due to a technical problem, and the displacement transducer fell out of service after 80 and 20 days, respectively. For test 1, the mini-pressure sensor fell out of service upon hydration (Table 6).

3.3. Dismantling protocol

The three tests (Table 6) were dismantled after more than 290 days of hydration. The hydration lasts for 315, 299, and 290 days for test 1 (sample SW), test 2 (sample A), and test 3 (sample S), respectively. After the hydration was stopped, the lid (Fig. 2*a*) was unscrewed and lifted off and the bridge-shaped structure containing the displacement transducer (Fig. 2*b*) was removed. Then, the screws securing the sample holder to the thick base were unscrewed and the hollow cylinder was removed from the base allowing the recovery of the samples for detailed characterization (Fig. 2*b*). For each of the three tests, the sample total diameter was measured using a caliper. After that, one half-sample was divided into three layers using the wire saw: layer a, which is the top layer; layer b, which is the middle layer; and layer c, which is the bottom layer (Fig. 3*b*). The thickness of the three layers was approximately the same. Moreover, each layer was divided into five subsamples (Fig. 3*a*). A detailed characterization of the 45 subsamples was conducted to determine the petrophysical parameters, mineralogy, and pore size distribution. In the

Table 6. The tree tests considered in this study.

Test	Solution	Sample	Lateral pressure sensor	Mini-pressure sensor	Displacement transducer	Fracture opening
1	Synthetic water	SW	Yes	Yes—out of service when launching the hydration	Yes	1.3 mm
2	Hyperalkaline solution	A	Yes	No	Yes—out of service after 80 days	1.5 mm
3	Saline solution	S	Yes	No	Yes—out of service after 20 days	1 mm

Fig. 3. (*a*) Top view. (*b*) Cross view of a half-sample after dismantling.

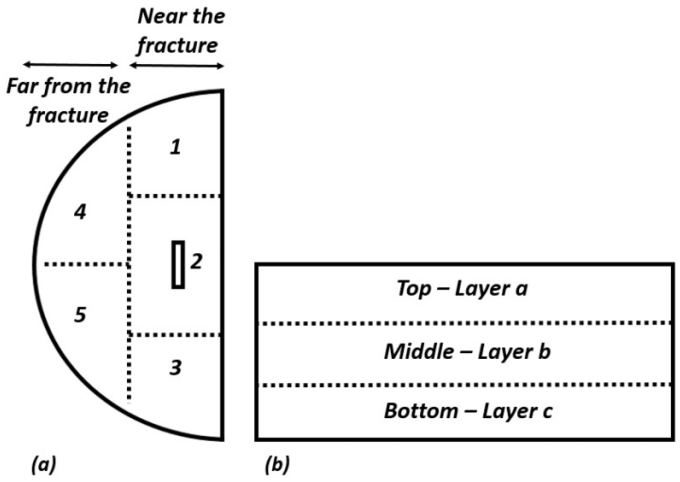

following, the subsamples will be named $X - Y - Z$, where X is the sample name (SW, A, or S in reference to synthetic water, alkaline, saline), Y is the layer (a, b, or c), and Z is the position (1, 2, 3, 4, or 5).

3.4. X-ray diffraction studies

To study the impact of alkalinity and salinity on the mineralogy of the LSF Opalinus Clay after more than 290 days of exposure, XRD measurements were performed on 16 subsamples from the three exposed samples and on five samples at initial state. XRD measurements were performed on 1 g disoriented powder by means of a PANalytical X'Pert Pro with Cu Kα ($\lambda = 1.54060$ Å) radiation operating at 40 kV, 30 mA, and 600 W. A nickel filter was placed at the rear to remove unwanted radiation such as Kβ line and continuous radiation from the X-ray beam. The divergence was set at 1/4 and a 20 mm mask was used to control the irradiated width on the sample. The angular interval varied from 2° to 64° in steps of 0.02°/s and the low knife mode was adopted, allowing a start angle less than 5°.

3.5. MIP and nitrogen adsorption/desorption tests

To explore the impact of pH and osmotic suction at microstructural scale, MIP and nitrogen adsorption/desorption tests were carried out on subsamples from the three exposed LSF Opalinus Clay samples (Table 7). MIP tests were performed on an AutoPore IV 9500 (Micromeritics Instrument Corp.) porosimeter at a controlled ambient temperature of 20 ± 1 °C. The applied mercury pressure ranged between 3 kPa and 227 MPa, allowing identification of entrance pore diameters between 343 μm and 5 nm (e.g., Sun and Cui 2020). To optimize the preservation of microstructure during water freezing, instantaneous freezing was carried out by plunging small cubic-shaped samples in slush nitrogen (−210 °C) obtained by previously submitting nitrogen to vacuum (e.g., Delage et al. 2006). The specimens were then placed in a freeze dryer for 24 h. To complement the pore size distribution at low pore sizes, nitrogen adsorption/desorption tests were carried out on a Micromeritics 3D flex device. The relative pressure of the nitrogen ranged between 0.1 and 0.39, allowing the entrance pore diameters between 57 and 3.2 nm to be identified based on the Barrett–Joyner–Halenda (BJH) approach. Analyzing the nitrogen adsorption isotherm data and applying the Brunauer–Emmett–Teller approach (e.g., Brunauer et al. 1938) allowed the determination of the specific surface area.

4. Results and discussions

4.1. Self-sealing test results

4.1.1. Radial swelling pressure

The evolution of the radial swelling pressure with time is presented in Fig. 4. For sample SW exposed to the synthetic water (pH = 7.5 and $\pi = 1$ MPa), the fluctuations in the radial swelling pressure observed for the first 120 days are probably not physical but due to the variation of the supply voltage. At 120 days, the radial swelling pressure started to increase (from −0.03 to 0.136 MPa at 265 days). Then, a slight decrease to 0.115 MPa was observed at 305 days. After that, the radial swelling pressure reincreased to 0.135 MPa at 315 days. As for the sample exposed to the saline solution (pH = 7 and $\pi = 34$ MPa), no significant swelling pressure was recorded even after 290 days of exposure. Finally, focusing on the sample exposed to the hyperalkaline solution (pH = 13.5 and $\pi = 1.16$ MPa), the swelling pressure varies nonmonotonically. Indeed, while an abrupt increase from 0 to 0.087 MPa was recorded in the first 45 days, a second but less pointy increase was logged (0.140 MPa at 147 days) before the swelling pressure started to decrease (0.075 MPa at 299 days).

Table 7. Fracture opening after dismantling.

Test	Solution	Sample	Fracture opening before exposure	Days of exposure	Fracture opening after exposure
1	Synthetic water	SW	1.3 mm	315	1 mm
2	Hyperalkaline solution	A	1.5 mm	299	1.4 mm
3	Saline solution	S	1 mm	290	0.3 mm

Fig. 4. Swelling pressure evolution with time.

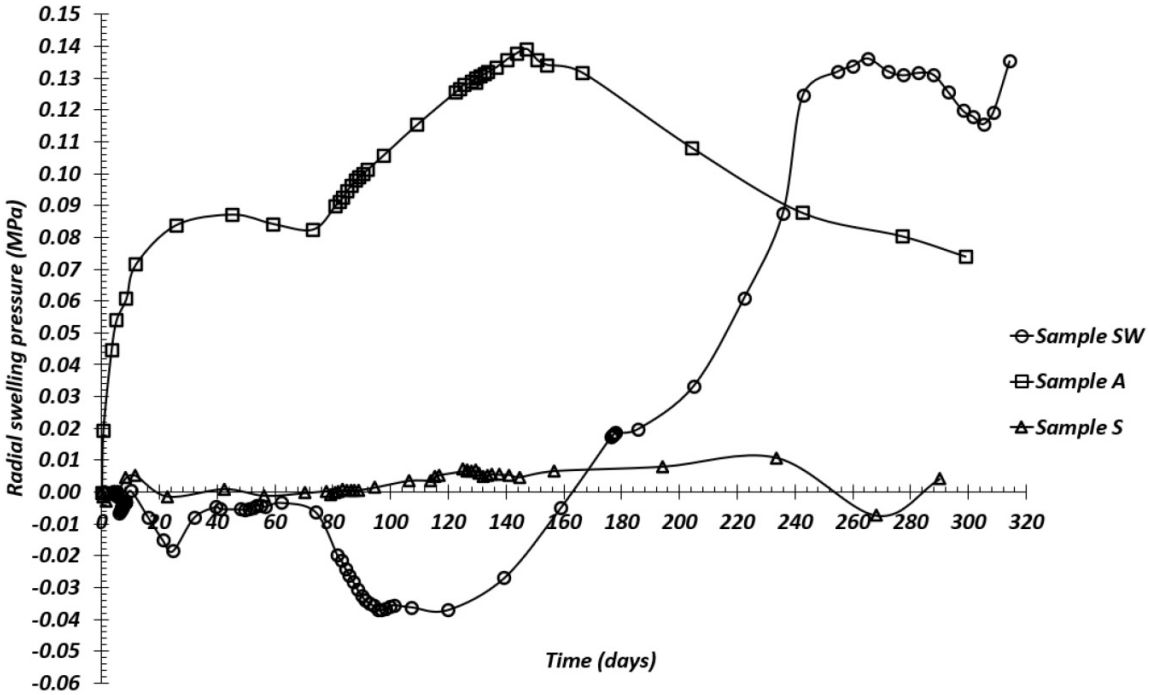

4.1.2. Fracture closure

The evolution of the displacement of the fracture opening (closure) with time is presented in Fig. 5. For the sample exposed to the synthetic water (pH = 7.5 and π = 1 MPa), almost 94% (0.23 mm) was recorded during the first 4 days (Fig. 5*b*). At this stage, the evolution of the displacement with time took a staircase shape (Fig. 5*a*) because the acquisition system did not record enough decimals. Based on this observation, the acquisition system was modified for the rest of the test. After 318 days, the displacement reached a value of 0.245 mm. As for the samples exposed to the hyperalkaline solution (pH = 13.5 and π = 1.16 MPa) and to the saline solution (pH = 7 and π = 34 MPa), negative values of displacement were logged in the first hours (Fig. 5b) suggesting a spreading of the blades of the displacement transducer. After that, the fracture closing was initiated and increases in displacements up to 0.035 and 0.015 mm were logged for the alkaline solution and the saline solution, respectively. After 80 and 20 days, the displacement transducers of tests 2 (alkaline) and 3 (saline) (Table 6), respectively, were out of service either because of a waterproofing problem at the blades level (i.e., the silicone comes off in a humid environment) or because of a chemical attack problem since the solutions are either very high pH or contain a lot of salt. The real cause is not yet defined.

4.1.3. Swelling pressure within the fracture

For test 1 (synthetic water) (Table 6), the mini-pressure sensor inserted within the fracture fell out of service directly after hydration because it was short-circuited due to water infiltration. For this reason, tests 2 and 3 were launched without this sensor.

4.2. Self-sealing test discussion

Several factors affected the overall self-sealing behavior. First, the friction forces mobilized between the top lid and the bottom base and the sample faces, whose magnitude depends on the swelling potential of the Opalinus Clay. In some cases, a small gap (0.1−0.2 mm) remained between the top lid and the sample, which may have affected both the friction forces and the radial swelling pressure magnitudes. Second, the presence of the mini-pressure sensor within the fracture hampered its self-sealing. Indeed, given the stiffness of the Opalinus Clay (Young's modulus parallel to bedding 7200 MPa, e.g., Bossart and Thurry 2008), the mini-pressure sensor within the fracture (Fig. 2), with a thickness of 0.6 mm, probably limited the fracture closure to ≈0.25 mm for test 1. For the test with the hyperalkaline solution (test 2), the values recorded by the displacement transducer varied insignificantly after 8 days (0.235 mm) (Fig. 5*a*), while the radial swelling pressure increased from 0.06 MPa

Fig. 5. (*a*) Displacement evolution with time and (*b*) a zoom on the first 10 days.

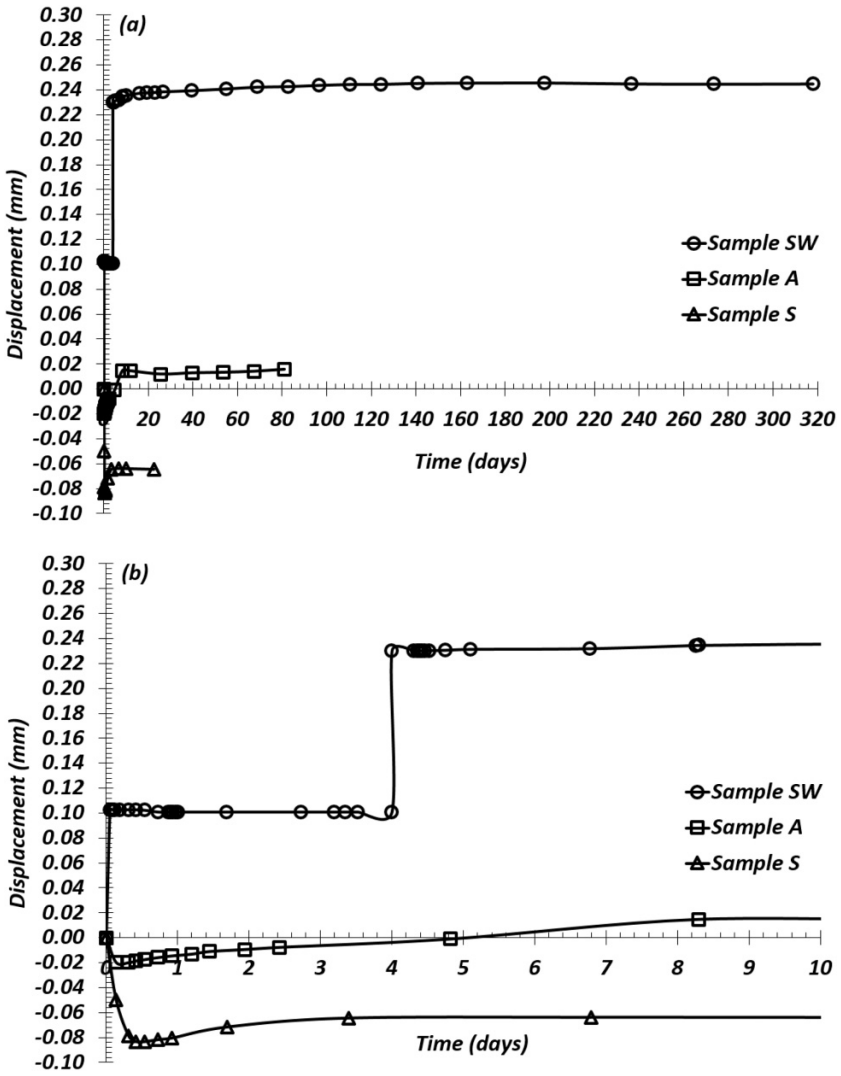

(at 8 days) to 0.082 MPa (at 40 days) (Fig. 4). Since no mini-pressure sensor within the fracture was installed for this test (Table 6), it is suspected that the friction forces exerted by the lid on the sample hampered the closure of the fracture. The decrease in swelling pressure recorded after 147 days suggests that the friction forces (0.053 MPa) were exceeded (Fig. 4), and that the half-sample was pushed toward the center. In this case, an increase in fracture closure was expected.

4.3. Dismantling

4.3.1. Observations

Figures 6–8 show the photos taken during the dismantling of tests 1, 2, and 3, respectively (Table 6). For test 1 (sample SW), prints of the mini-pressure sensor inserted inside the fracture are observed on the sides of both sample halves (Figs. 6*c* and 6*d*). The prints of the screws dedicated to fixing the bottom porous stone to the cell base (Fig. 2*b*) are also observed on the bottom of samples SW and A (Figs. 6*e* and 7*c*) supporting the assumption of high friction forces. For tests 1 (sample SW) and 2 (sample A), no fractures were detected with the naked eye (Figs. 6 and 7). However, for test 3 (sample S), a fracture was detectable on top of the sample (Fig. 8*a*) and particle detachment was observed on the side of the left half-sample (Fig. 8*c*). The fracture opening after dismantling obtained by measuring the total diameter with a caliper is reported in Table 7. A fracture closing of 0.3 mm (23%), 0.1 mm (6%), and 0.7 mm (30%) was recorded for samples SW, A, and S, respectively. These results agree with those reported in Figs. 4 and 5. For sample A, an unsignificant displacement (10 orders of magnitude lower compared with SW) was recorded by the displacement transducer before it fell out of service (Fig. 5). The value of closure of the fracture measured after dismantling indicates that the expected displacement at 140 days (upon radial swelling pressure decrease) has occurred. For sample S, a fracture closing of 0.7 mm was measured (Table 7). This result supports the hypothesis that the higher the swelling pressure, the higher the friction and the smaller the fracture closing. Indeed, the low swelling pressure induced by the high salinity (Zhu et al. 2013; Ye et al. 2015; Chen et al. 2017) implied low friction, promoting the fracture self-sealing. For sample

Fig. 6. Photos taken during the dismantling of test 1 (sample SW): (*a*) after unscrewing the lid and removing the bridge-shaped structure; (*b*) after extracting the sample; (*c*) right half-sample seen from front; (*d*) right half-sample seen from bottom; (*e*) left half-sample seen from front.

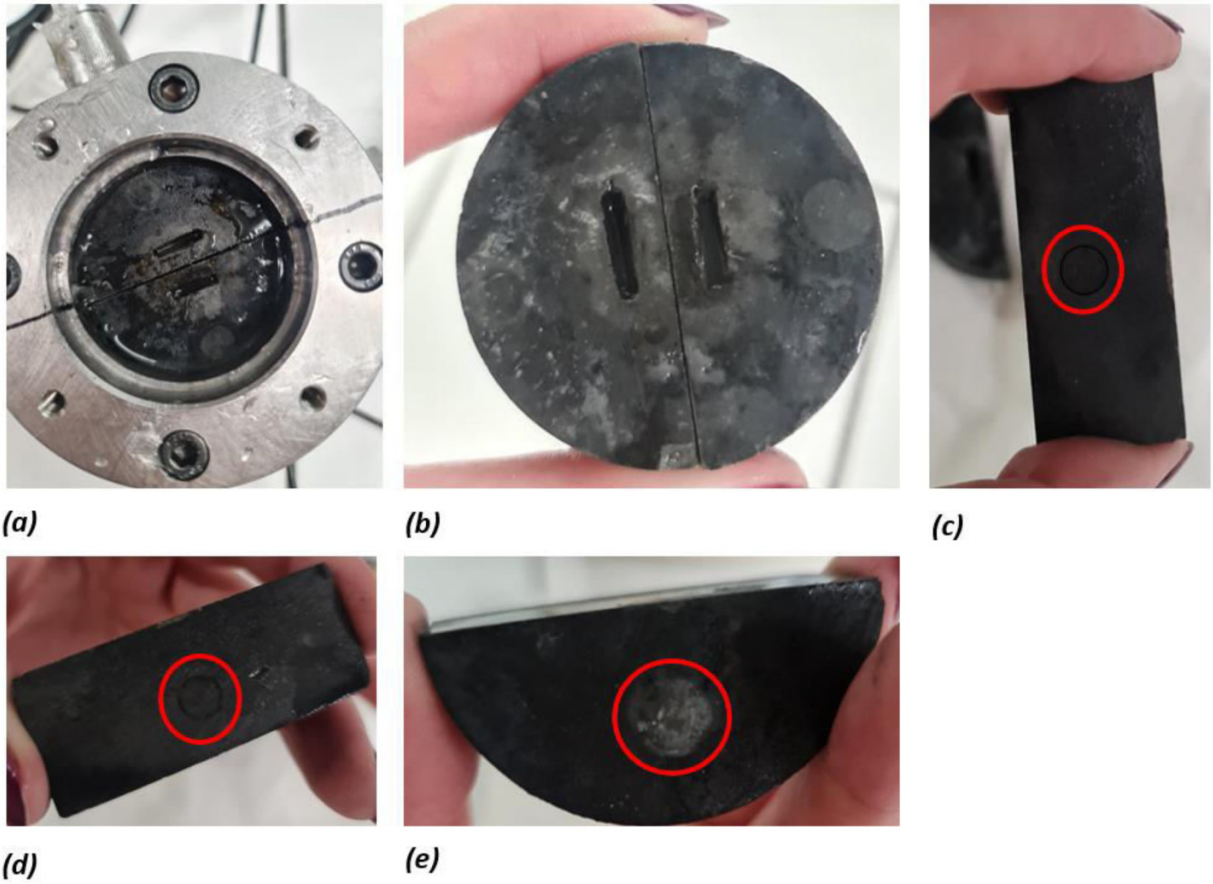

Fig. 7. Photos taken during the dismantling of test 2 (sample A): (*a*) after unscrewing the lid and removing the bridge-shaped structure; (*b*) left half-sample seen from above; (*c*) right half-sample seen from above.

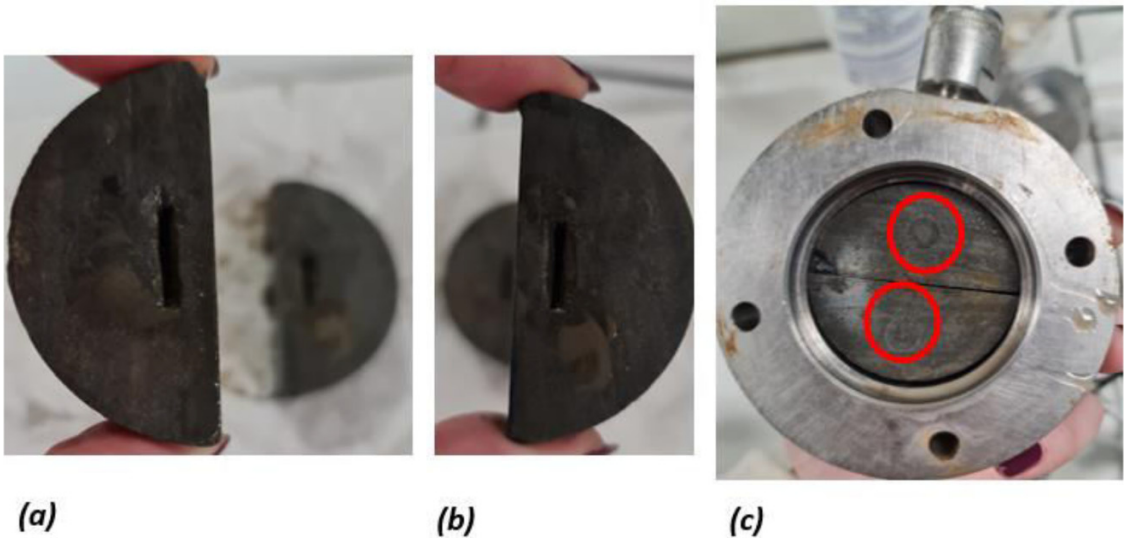

SW, since the swelling potential was expected to be higher than that of sample S, if the friction and the mini-pressure sensors were absent, the fracture self-sealing would be more significant.

4.3.2. Petrophysical parameters

Figure 9 shows the variation of the petrophysical parameters via the three layers of 30 subsamples taken from sam-

Fig. 8. Photos taken during the dismantling of test 3 (sample S): (*a*) after unscrewing the lid and removing the bridge-shaped structure; (*b*) after extracting the sample; (*c*) left half-sample seen from front.

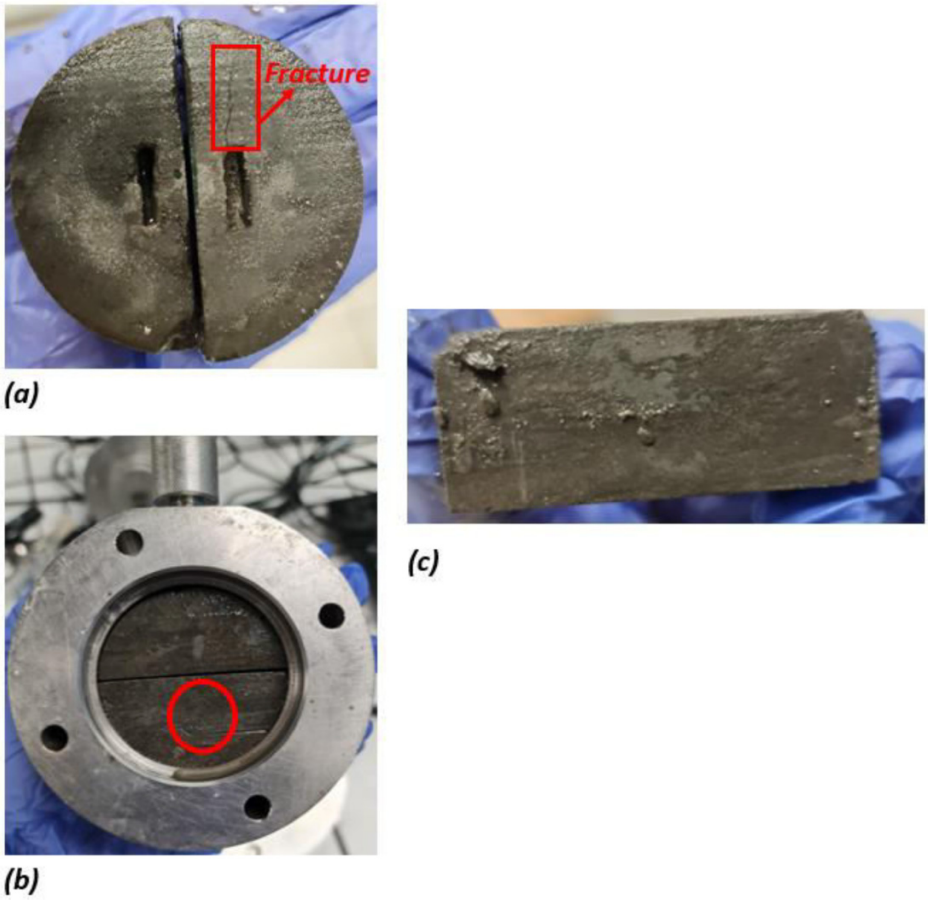

ples SW and A (Table 6) at different positions (Fig. 3) together with the initial petrophysical parameters of the dry investigated core (Table 2). The average values measured near and far from the fracture are shown in Fig. 10. The water content, initially ranging from 0.89% to 1.66% (Table 2), increased with hydration for both samples, but to a lesser extent for sample W (Fig. 9*a*). Indeed, for this sample, the water content is comprised between 1.26% and 2.34% with an average value of 1.63%. The lowest and highest water contents were both measured at the bottom layer (layer c) (Figs. 3 and 9*a*), and, on average, the top layer (layer a) % (Fig. 3) was more hydrated than both middle (layer b) ($w = 1.4\%$) and bottom layers (layer c) ($w = 1.6\%$) (Fig. 9*a*). These low water contents explain, together with the presence of the mini-pressure sensor within the fracture (Table 6) and the friction, why the fracture closing (0.245 mm) stopped evolving with time (Fig. 5*a*). Indeed, for this test, the claystone was not well hydrated. This may be due to the trapping of air, initially present in the pores of the dry sample, inside the cell. The low water contents also explain the low swelling pressure (0.166 MPa) reached after 315 days of hydration (Fig. 4). For sample A, the water content is comprised between 2.54% and 5.28% with an average of 3.54%. Surprisingly, the lowest and highest water contents were both found in the middle layer (layer b) (Fig. 9*a*), suggesting the presence of nonvisible microfractures that favored the hydration of the central zone. Also, on average (w = 3.4%, 4%, and 3.2% for layers a, b, and c, respectively), higher water contents were found for the middle layer (layer b) and near the fracture for the three layers (Fig. 10*a*). From Figs. 9*a* and 10*a*, it appears that sample A was more hydrated than sample SW even though sample SW was hydrated for a longer period (Table 7) and the solution outlets were closed for both tests. Figures 9*b* and 9*c* show the calculated dry densities and void ratios of the 30 subsamples taken from samples SW and A (Table 6). The measured range of the dry density, initially 2.26–2.43 Mg/m^3 ($e = 0.11-0.2$) (Table 2), varied to 2.31–2.48 Mg/m^3 and to 2.12–2.28 Mg/m^3 for samples SW and A, respectively, with a tendency to decrease for the alkaline case. For sample A, the void ratio reached a maximum value of 0.28 (2.12 Mg/m^3) in the bottom layer (Fig. 9*c*) and a decrease in the average value was observed when moving to the top layer (layer a) (Fig. 10*c*). Higher void ratios were recorded near the fracture for layer b (Fig. 10*c*), which agrees with the water content distribution (Fig. 10*a*). For the average dry density (Fig. 10*b*), no significant variation was found far from the fracture between the three layers. These results confirm the presence of several hydration sources for the alkaline case: the two facets of the fracture and the sample bottom together with the possible existence of microfractures that favored the hydration of the middle part. For sample

Fig. 9. Petrophysical parameter variation through the layers for samples SW, A, and S. (*a*) Water content. (*b*) Dry density. (*c*) Void ratio. (*d*) Degree of saturation.

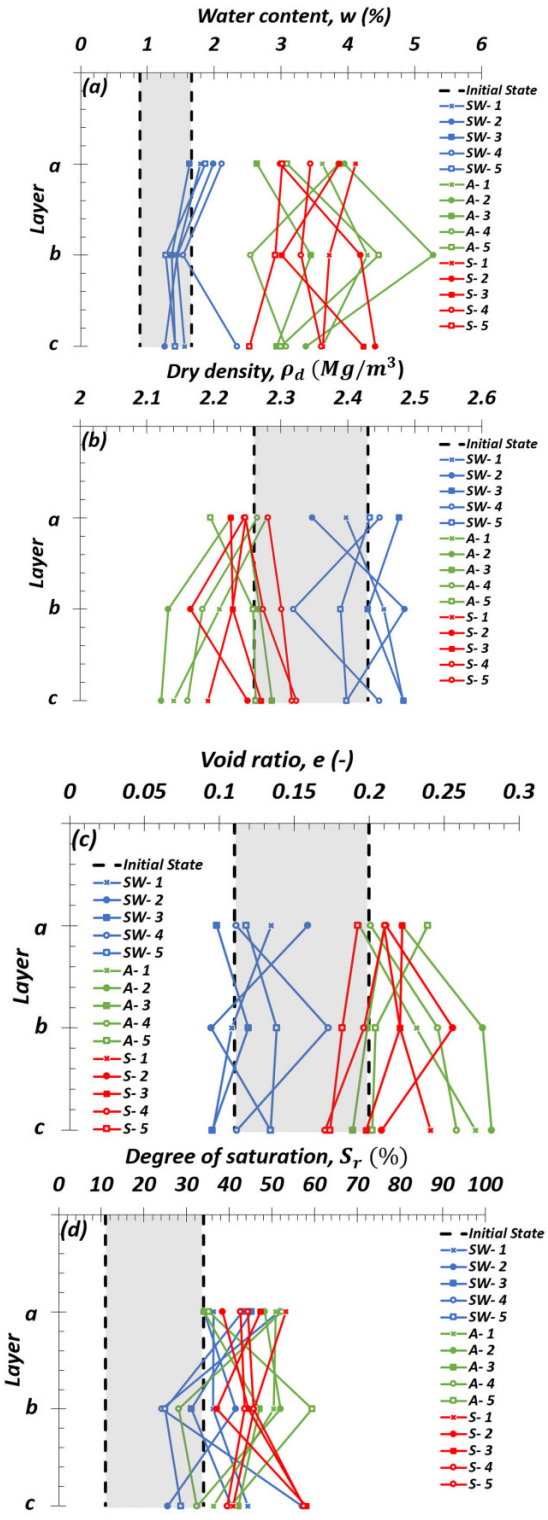

Fig. 10. Petrophysical parameter (average of positions 1,2,3 (near the fracture) and average of positions 4,5 (far from the fraction)) variation through the layers for samples SW, A, and S. (*a*) Water content. (*b*) Dry density. (*c*) Void ratio. (*d*) Degree of saturation.

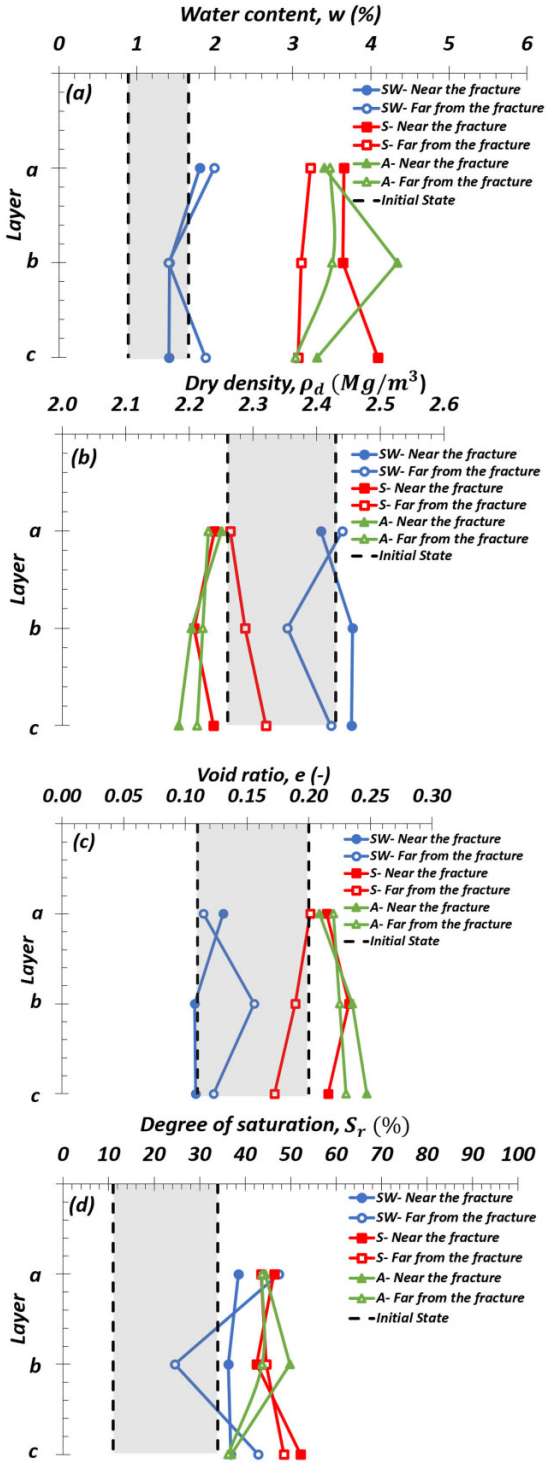

SW, the void ratio reached a minimum value of 0.09 in the bottom layer (Fig. 9*b*). Lower void ratios (higher dry densities) were recorded near the fracture for layers b and c (Figs. 10*b* and 10*c*). This decrease might be due to the local compression of the material in the vicinity of the mini-pressure sensor. Indeed, Fig. 5*a* shows the stabilization of the fracture opening after 4 days with no variation of the radial swelling pressure until 120 days (Fig. 4), which suggests that a swelling pressure was exerted on the mini-pressure sensor between 4 and

Fig. 11. X-ray diffraction profiles of five LSF Opalinus Clay samples from the investigated core at initial state and six subsamples from sample SW. I, illite; K, kaolinite; Ch, chlorite; Q, quartz; C, calcite.

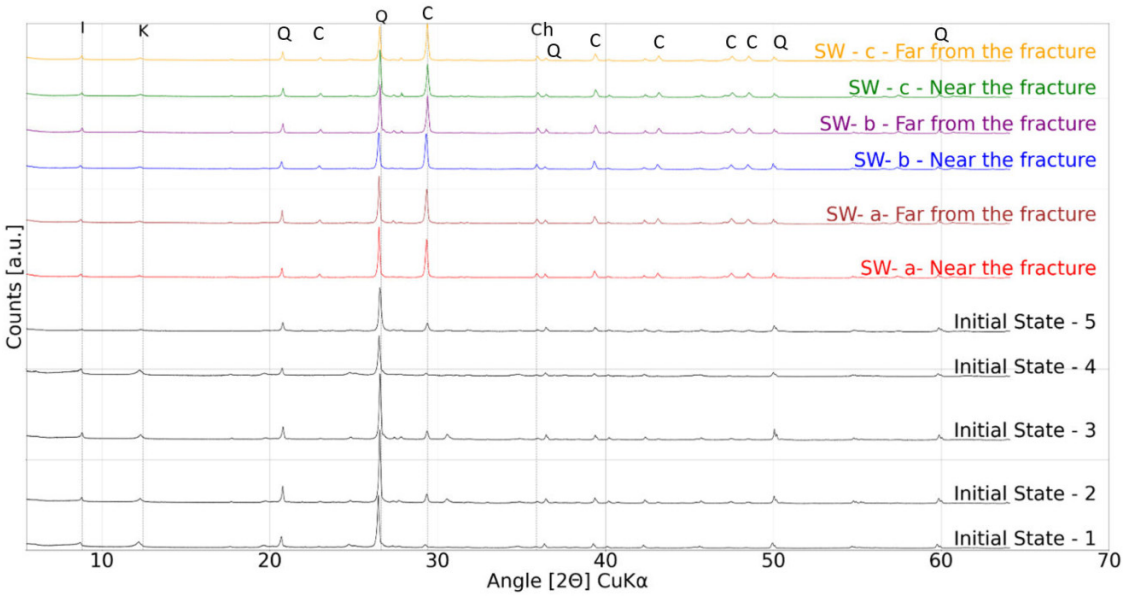

120 days. This could have led to local compression of the two half-samples. Figure 9*d* shows an increase in the degree of saturation for both samples compared with the initial range (11%–34%) (Table 2). Since the water content of sample A is higher than that of sample SW (Figs. 9*a* and 10*a*) with the first sample being less dense (Figs. 9*b* and 10*b*), it is difficult to conclude which one was more saturated. However, on average, the top and middle layers were more saturated for sample A than W (Fig. 10*d*).

Figure 9 also shows the variation of the petrophysical parameters of 15 subsamples taken from sample S (Table 6). The average values are also presented in Fig. 10. The water content, initially between 0.89% and 1.66% (Table 2), increased with hydration to reach values ranging from 2.52% to 4.41%, and, on average, $w = 3.5\%$, 3.4%, and 3.6% for layers a, b, and c, respectively. The sample exposed to the saline solution appears to be more hydrated than sample SW even though the hydration period for the latter was longer (Figs. 9*a* and 10*a*). In addition, higher water contents were found for the subsamples taken near the fracture (Fig. 10*a*). Indeed, the secondary fracture observed on the top of sample S upon dismantling (Fig. 8*b*) may have constituted an additional flow path that enhanced the hydration. This fracture might have been generated by the shrinkage of the diffuse double layer under high osmotic suction. Even though the swelling magnitude is expected to decrease due to the increase of osmotic suction, the fast hydration of sample S probably resulted in a relatively rapid decrease of matric suction (in comparison to sample SW) inducing the swelling of the partially saturated sample. This phenomenon explains the significant decrease of the fracture opening in the case of saline solution compared with the other two tests where the high friction (samples A and SW), the insertion of the mini-pressure sensor within the fracture, and the low hydration state (sample SW) hampered the closing of the fracture (Table 7). Finally, comparing S and A results (Figs. 9*a* and 10*a*), it appears that both samples have reached the same water content range, confirming the possible existence of microfractures that may have promoted the hydration of the middle layer of sample A (Figs. 9*a* and 10*a*). However, since no significant self-sealing was observed in this case, it can be inferred that the friction between the sample faces and the top and bottom lids was the highest. Figures 9*b* and 9*c* show the dry densities and the void ratios of the 15 subsamples taken from sample S (Table 6). The dry density, initially equal to 2.26–2.43 Mg/m^3, decreased to 2.16–2.32 Mg/m^3, with a more significant decrease near the fracture (Figs. 9*b* and 10*b*), which agrees with the water content distribution (Figs. 9*a* and 10*a*). These results suggest that a more significant swelling occurred near the fracture. Comparing the results of samples A and S, it appears that the decrease of the dry density (increase of void ratio) was more significant in the former case (Figs. 9*b* and 10*b*), suggesting a more significant swelling. Figures 9*d* and 10*d* show an increase in the degree of saturation of sample S compared with the initial range (11%–34%) (Table 2). The middle (S_r = 45% and 30% for samples S and SW, respectively) and bottom (S_r = 44% and 40% for samples S and SW, respectively) layers were more hydrated in sample S compared with SW. Since the water content of sample S is higher than that of sample SW (Figs. 9*a* and 10*a*) with the first sample being less dense (Figs. 9*b* and 10*b*), it is difficult to conclude which one was more saturated.

4.3.3. XRD measurements

Figure 11 shows the XRD profiles of five LSF Opalinus Clay samples from the investigated core at initial state together with the XRD profiles of six subsamples taken from the three layers of sample SW near and far from the fracture. The

Fig. 12. X-ray diffraction profiles of five LSF Opalinus Clay samples from the investigated core at initial state and five subsamples from sample A. I, illite; K, kaolinite; Ch, chlorite; Q, quartz; C, calcite.

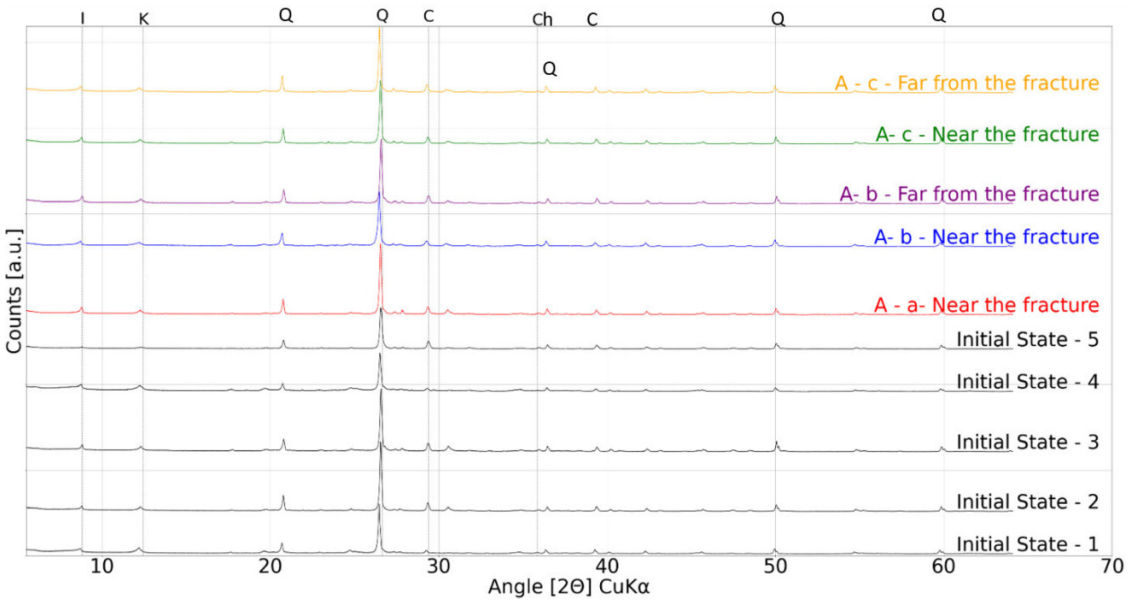

Fig. 13. X-ray diffraction profiles of five LSF Opalinus Clay samples from the investigated core at initial state and five subsamples from sample S. I, illite; K, kaolinite; Ch, chlorite; Q, quartz; C, calcite.

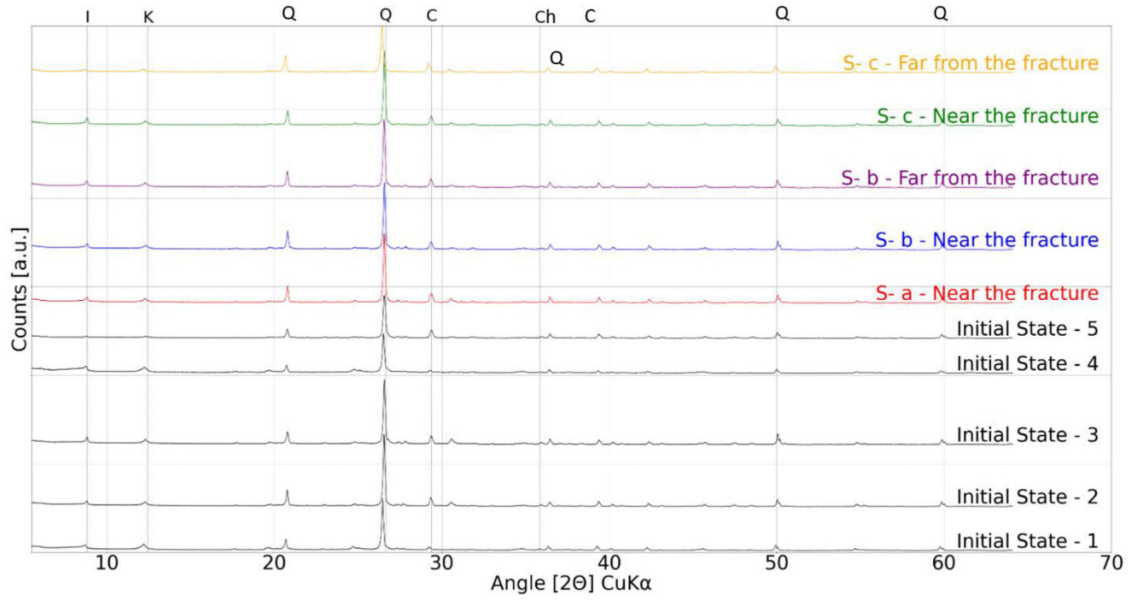

five samples at initial state contain the same minerals (calcite, illite, kaolinite, quartz, and chlorite). However, the intensities of the peaks at 20.850 2θ, 26.652 2θ, 50.141 2θ and 29.406 2θ, 39.402 2θ corresponding to quartz and calcite, respectively, vary among the five samples. Indeed, sample 1 and sample 4 do not contain as much calcite as the other three samples. The quartz content also varies significantly between the five samples. Illite and kaolinite contents also vary, but in a less pronounced way. These observations underline the significant heterogeneity of the sandy facies of the Opalinus Clay in terms of mineralogy (Lerouge 2014; Ould Bouya 2014; Lauper et al. 2018; Kneuker and Furche 2021). In addition to the previous observations, it appears that the quartz content slightly varies between the six subsamples exposed to the synthetic water (see peak at 26.652 2θ). Comparing these results to those at initial state, it seems that the variation of the intensities of the peaks corresponding to quartz is due to the variability of the mineralogy of the LSF Opalinus Clay (Fig. 11). The calcite content does not seem to vary between the six subsamples. However, a significant increase of the intensities of the peaks at 23.022 2θ, 29.406 2θ, 39.402 2θ, 43.146 2θ, 47.490 2θ, 48.514 2θ corresponding to

calcite is observed with respect to the initial state (Fig. 11). Unlike quartz, this increase is not due to the heterogeneity of the LSF Opalinus Clay since new peaks corresponding to calcite (23.022 2θ, 43.146 2θ, 47.490 2θ, 48.514 2θ), that were not detected at initial state, appeared after exposure to the synthetic water (Fig. 11). This increase in calcite content is due to the dissolution of the CO_2 from air into the synthetic water already containing Ca^{2+} ions (Tables 2 and 4). Indeed, the CO_2 from air dissociates into hydrogen carbonate ions for pHs around neutral according to the following equation:

$$(2) \quad CO_{2(aq)} + H_2O_{(l)} \rightarrow HCO^-_{3(aq)} + H^+_{(aq)}$$

The hydrogen carbonate ions associate with Ca^{2+} ions from the synthetic water following eq. 3 and calcite precipitation occurs.

$$(3) \quad HCO^-_{3(aq)} + Ca^{2+}{}_{(aq)} \rightarrow CaCO_{3(s)} + H^+_{(aq)}$$

The resulting equation is as follows:

$$(4) \quad CO_{2(aq)} + H_2O_{(l)} + Ca^{2+}{}_{(aq)} \rightarrow CaCO_{3(s)} + 2H^+_{(aq)}$$

Calcite precipitation probably explains (together with the local compression mechanism) the increase in dry density (decrease in void ratio) observed for the subsamples taken from sample SW. It might also induce a decrease in the permeability of the sample, which explains the low water content and degree of saturation of sample SW (Figs. 9 and 10).

Figure 12 shows the XRD profiles of five LSF Opalinus Clay samples from the investigated core at initial state together with the XRD profiles of five subsamples taken from the three layers of sample A near and far from the fracture. It appears that the quartz content slightly varies between the five subsamples exposed to the hyperalkaline solution (see peak at 26.652 2θ). Comparing these results to those at initial state, it seems that the variation of the intensities of the peaks corresponding to quartz is due to the variability of the mineralogy of the LSF Opalinus Clay (Fig. 12). The calcite content does not seem to vary between the different exposed subsamples and with respect to the initial state. While calcite and quartz dissolutions are expected to occur after 290 days of exposure to a hyperalkaline solution (e.g., Barakat et al. 2022), this did not happen in this case. Unlike the testing conditions in Barakat et al. (2022), the sample was not fully saturated (Figs. 9*d* and 10*d*) and the solution/solid ratio was very small.

Figure 13 shows the XRD profiles of five LSF Opalinus Clay samples from the investigated core at initial state together with the XRD profiles of five subsamples taken from the three layers of sample S near and far from the fracture. It appears that the quartz content slightly varies between the five subsamples exposed to the $NaNO_3$ solution (see peak at 26.652 2θ). Comparing these results to those at initial state, it seems that the variation of the intensities of the peaks corresponding to quartz is due to the variability of the mineralogy of the LSF Opalinus Clay (Fig. 13). The calcite content does not seem to vary between the different exposed subsamples and with respect to the initial state. Indeed, unlike the synthetic water, the highly saline solution does not contain Ca^{2+} ions making calcite precipitation impossible.

Fig. 14. BJH density functions for sample SW. (*a*) Top layer. (*b*) Middle layer. (*c*) Bottom layer.

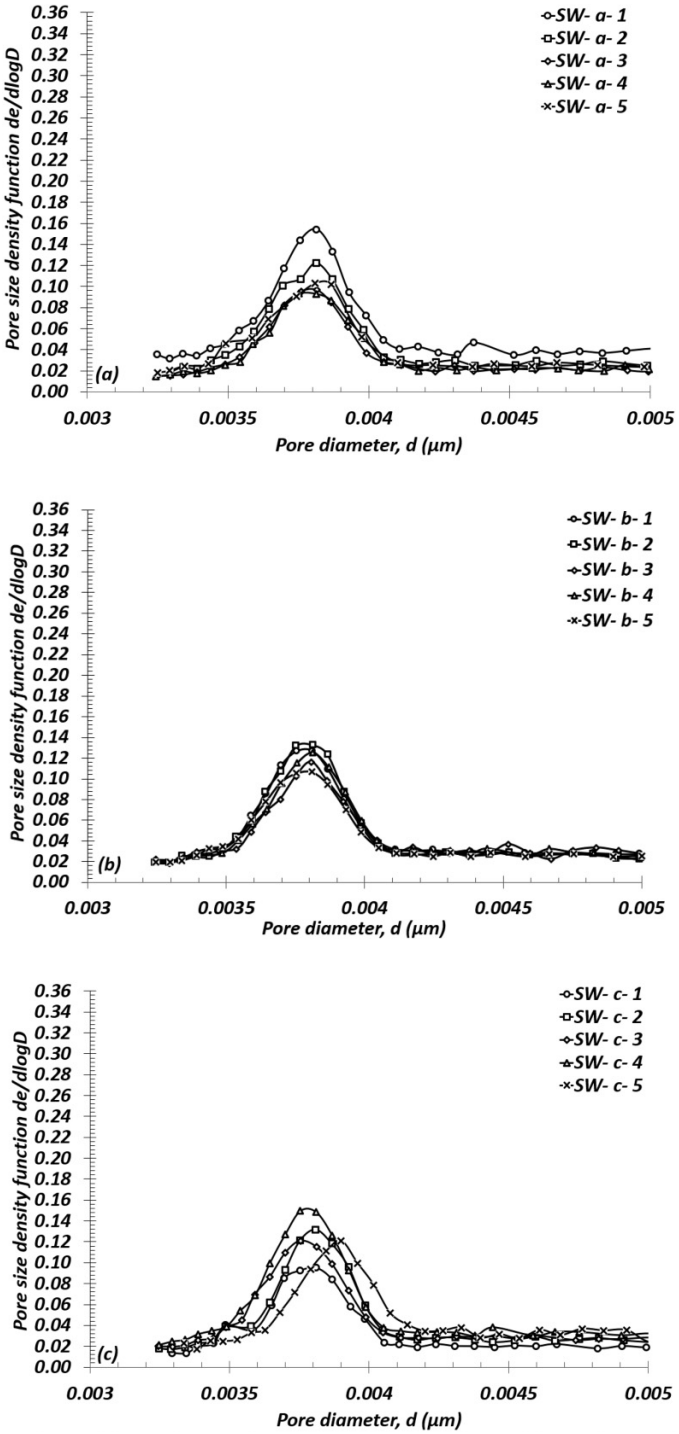

Fig. 15. Density functions for sample S. (*a*, *b*) Top layer. (*c*, *d*) Middle layer. (*e*, *f*) Bottom layer.

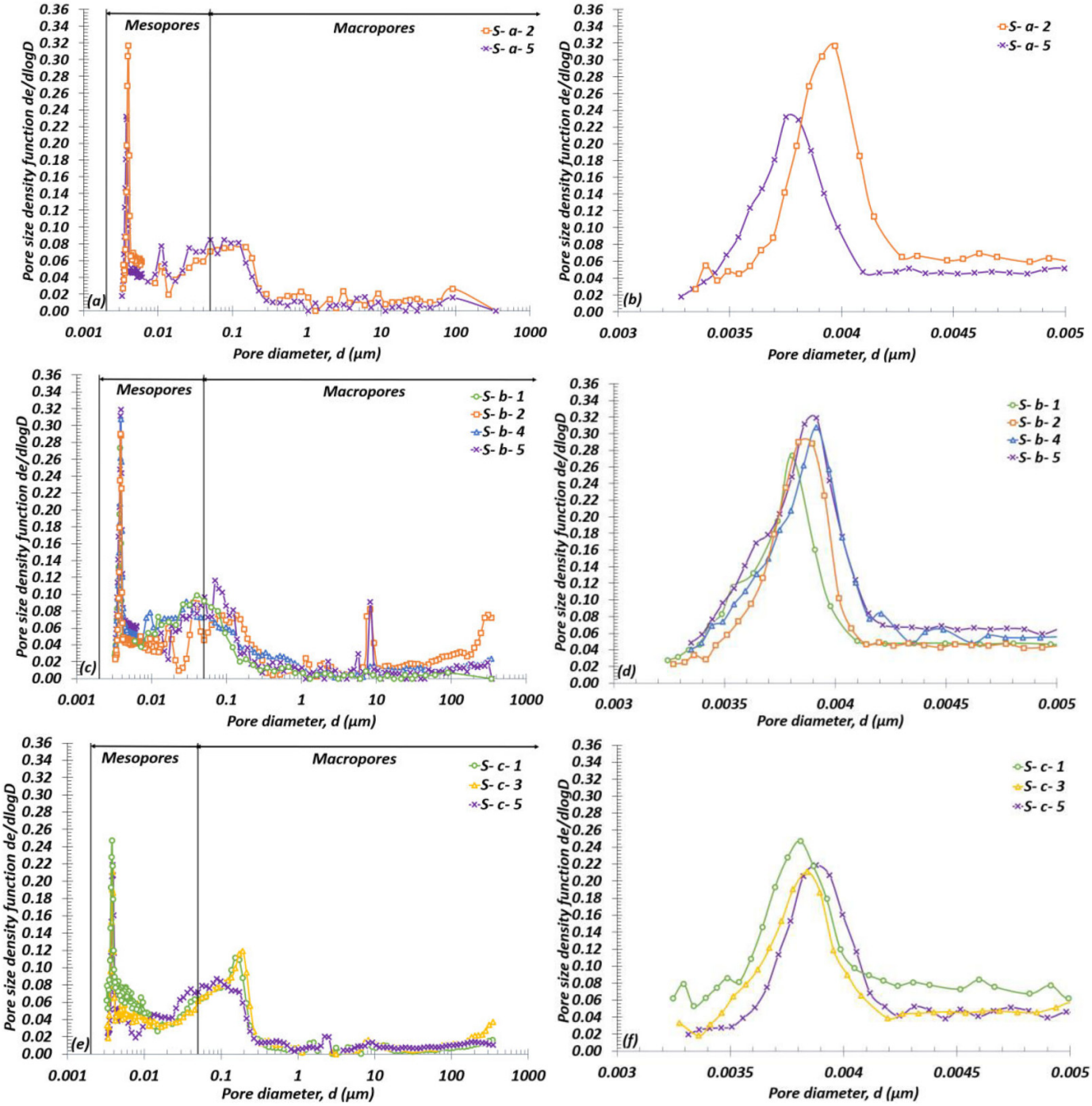

4.3.4. MIP and nitrogen adsorption/desorption tests

A total of 45 nitrogen adsorption/desorption tests were carried out on 45 subsamples from samples SW, S, and A (Table 6) (Figs. 14–17). However, the MIP tests (nine tests) were performed only on sample S (Fig. 15). The pore network of the LSF Opalinus Clay is mainly composed of macropores (pore size > 50 nm) and mesopores (2 nm < pore size < 50 nm) according to the International Union of Pure and Applied Chemistry classification (Sing 1991). Figure 14 shows the BJH density functions of the 15 subsamples from sample SW. Overall, higher densities of macropores or bigger macropores were found near the fracture for layer (Fig. 14*a*), suggesting that the higher the swelling, the more significant the generation of mesopores. For layer b, since the water contents vary insignificantly between $w = 1.3\%$ and $w = 1.5\%$ for the five positions, no significant differences in the pore size distribution were identified (Fig. 14*b*). For layer c, the highest (position 4) and biggest (position 5) pore diameters were found far from the fracture (Fig. 14*c*), in agreement with the

Fig. 16. BJH density functions for sample A. (*a*) Top layer. (*b*) Middle layer. (*c*) Bottom layer.

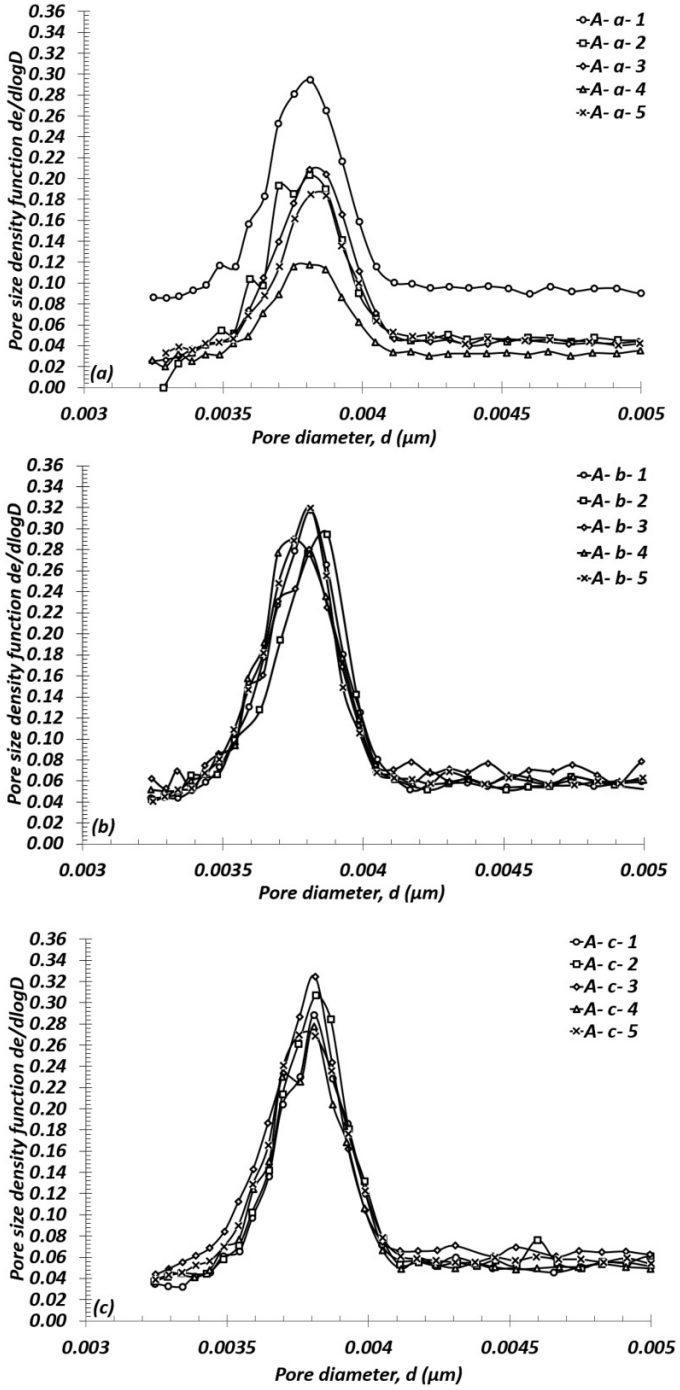

highest average water content found far from the fracture (Fig. 10*a*).

Figure 15 shows the pore size density (PSD) functions of sample S. Comparing the PSDs of S-a-2 and S-a-5 (Fig. 15*a*), since both subsamples have the same water content ($w = 3\%$), S-a-2, taken near the fracture, has a higher density of macropores >60 μm compared with S-a-5. Surprisingly, the S-a-2 has a higher mesopore density and bigger mesopores (Fig. 15*b*). The PSD of S-b-2 shows there are macropores larger than 100 μm (Fig. 15*c*). Note that for this test, fractures were detected with the naked eye after dismantling (Fig. 8*a*). The fractures are probably due to the increased swelling near the fracture and to the shrinkage of the diffuse double layer under salinity. Figures 15*d* and 15*f* show that subsamples taken far from the fracture have higher densities of the dominant mesopore family and/or bigger BJH peaks compared with the ones taken near the fracture, while Fig. 15*e* shows that higher densities of macropores were found near the fracture. Indeed, the fracture being a hydration front, higher swelling is expected near the fracture, leading to from where the higher values of higher water contents, higher densities of macropores, lower densities of mesopores and smaller BJH peaks.

Figure 16 shows the BJH density functions of the 15 subsamples from sample A. For the three layers, the subsamples taken near the fracture have either the biggest BJH peak or the highest density of mesopores. This is because the subsamples near the fractures were, on average, more hydrated (Fig. 10*a*). These results show that the density and/or the peak of mesopores increased with water content for sample A.

Figure 17 compares the BJH density functions of the 45 subsamples (samples SW, A, and S). It appears that the smallest BJH peak and density were constantly recorded for sample SW. This is probably due to the low water content in this case (Fig. 9*a*). For sample A, the acid–base attack probably occurred (e.g., Wahid et al. 2011*a*), resulting in a dispersed structure (Mitchell 1993; Wahid et al. 2011*a*, 2011*b*; Chavali et al. 2017) and higher repulsive forces between the clay particles (Mitchell 1993; Chavali et al. 2017), and thus the increase in the BJH peak and/or density compared with sample SW. For sample S, dispersion (e.g., Chorom and Rengasamy 1995) or flocculation (e.g., Pedrotti and Tarantino 2018) could occur depending on the saturation state. Dispersion will cause an increase in the BJH peak and/or density (e.g., Wilson et al. 2014), whereas flocculation will lead to a decrease in the mesopore population. For sample S, since the values of S_r were lower than 60% for all the subsamples (Fig. 9*d*), the flocculation was not initiated, which explains the increase in the BJH peak and/or density compared with sample SW (Fig. 17).

Figure 18 shows the specific surface area of the 45 subsamples (samples SW, A, and S). The smallest values were constantly recorded for sample SW due to its low water content. For samples A and S, since both samples have approximately the same water content (between 3% and 4%) (Figs. 9*a* and 10*a*), the higher specific surface areas, constantly recorded for the hyperalkaline solution, suggest that alkalinity increases the swelling potential of the LSF Opalinus Clay compared with saline solutions. These results agree with the dry density and void ratio distributions (Figs. 9*b*, 9*c*, 10*b*, and 10*c*).

5. Conclusions

In the present study, a new experimental device was used to monitor the self-sealing of swelling claystones. The material investigated was the LSF Opalinus Clay from Mont Terri site in Switzerland. Three solutions were used to simulate in situ conditions: a synthetic water (pH = 7.5, π = 1 MPa), a saline solution ($NaNO_3$, pH = 7, π = 34 MPa), and a hyperalkaline solution (pH = 13.5, π = 1.16 MPa). The fracture closing was monitored with a displacement transducer, and the

Fig. 17. BJH density functions for samples SW, A, and S. (*a*) Position 1, top. (*b*) Position 1, middle. (*c*) Position 1, bottom. (*d*) Position 2, top. (*e*) Position 2, middle. (*f*) Position 2, bottom. (*g*) Position 3, top. (*h*) Position 3, middle. (*i*) Position 3, bottom. (*j*) Position 4, top. (*k*) Position 4, middle. (*l*) Position 4, bottom. (*m*) Position 5, top. (*n*) Position 5, middle. (*o*) Position 5, bottom.

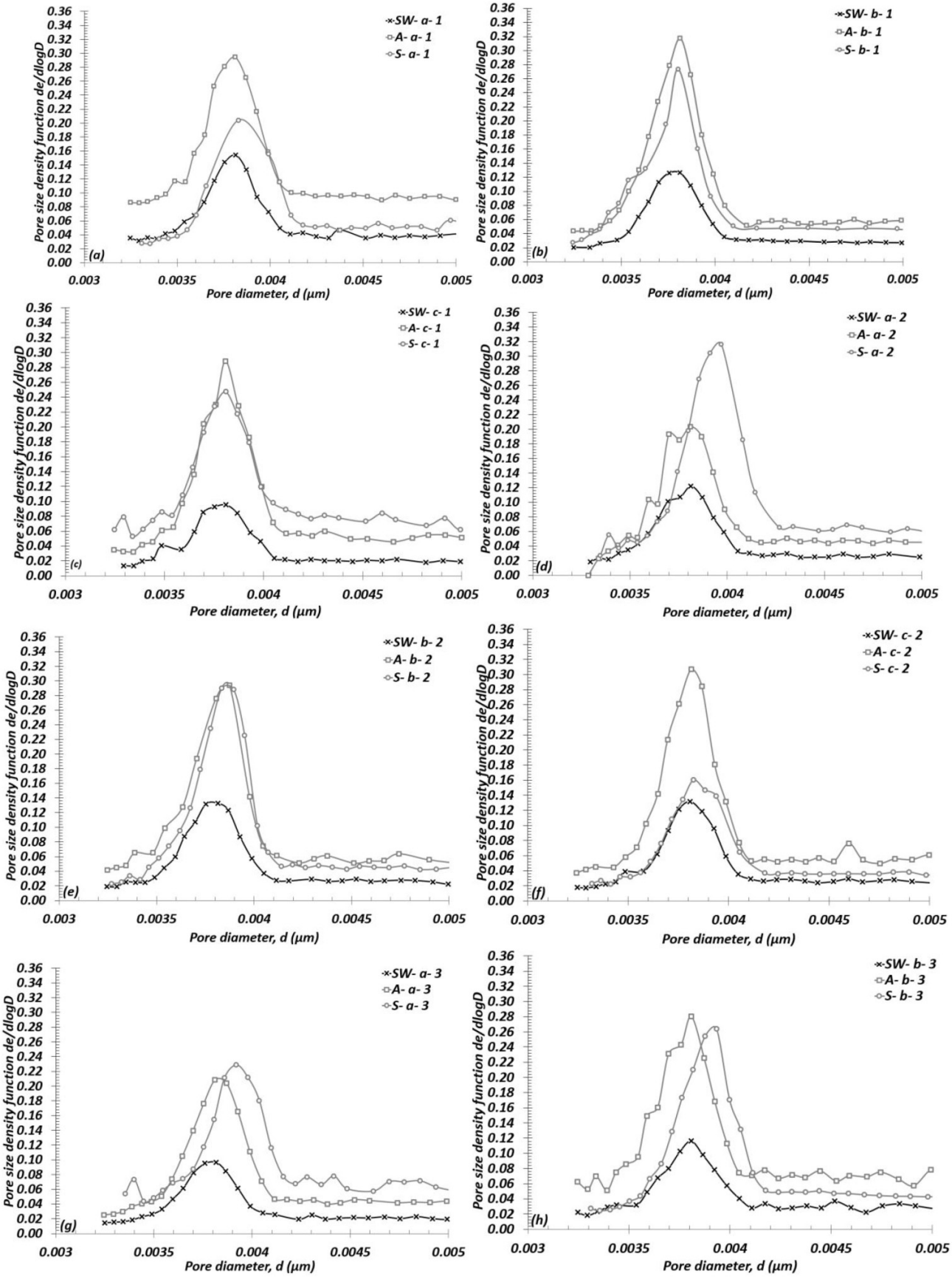

Fig. 17. (*Continued.*)

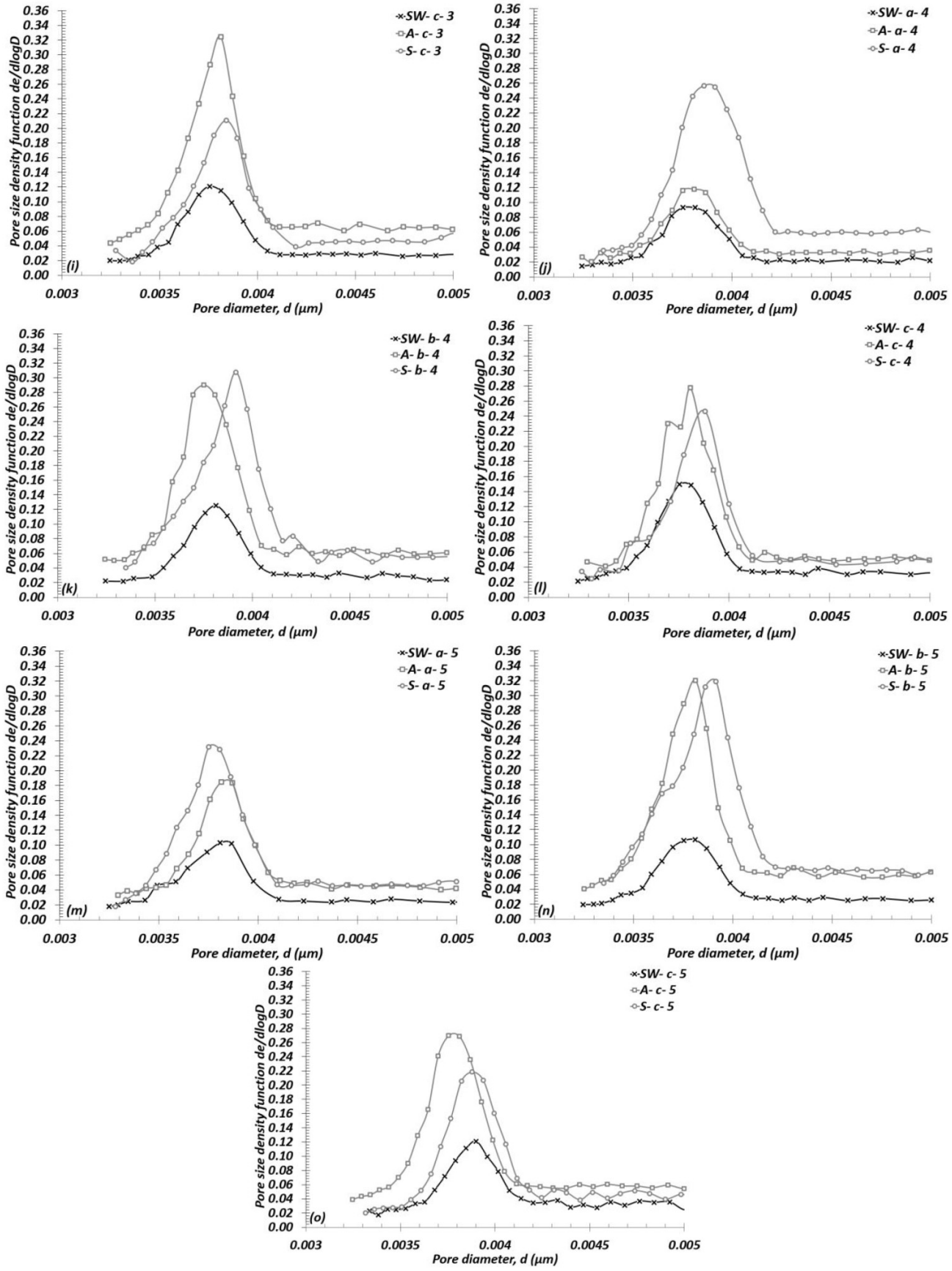

Fig. 18. Specific surface area for the 45 subsamples from samples SW, A, and S.

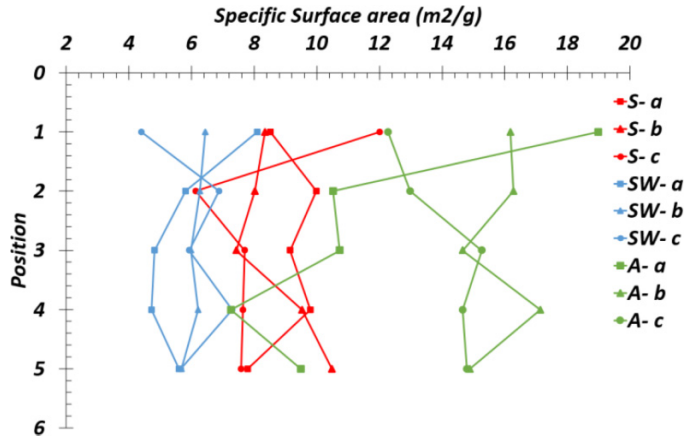

radial swelling pressure was monitored via a total pressure sensor. The three tests ran for over 290 days. After dismantling, a detailed petrophysical characterization was conducted for the three samples. The mineralogy and pore size distribution were also determined at different positions. Results show that, for this experimental setup, the friction forces exerted by the porous stones on the top and bottom of the samples are to be considered. They depend on the sample height, the installation protocol, and the swelling potential of the material. For the three tests, the fracture closing was limited due to several mechanisms. In the case of samples SW and A, the friction was significant, hampering the self-sealing of the fracture. In addition, in the case of sample SW, the presence of the mini-pressure sensor within the fracture that generated local compression, and calcite precipitation also contributed to limiting the fracture closing. In the case of sample S, even though the friction was not significant, the complete self-sealing did not happen because salinity decreased the swelling of the clay particles by reducing the thickness of the diffuse double layer.

Based on the petrophysical characterization and the pore size distributions of samples S and A, several hydration fronts were identified: the two facets of the fracture, the sample bottom and secondary fractures generated with hydration.

While salinity does not affect the mineralogy of the LSF Opalinus Clay, the contraction of the diffuse double layer due to salinity increase explains, together with the higher water contents, the observed microstructural changes. This mechanism contributed to the generation of secondary fractures within the sample increasing the sample permeability and accelerating the hydration process. For sample A, even though calcite and quartz dissolutions were not observed as expected (e.g., Barakat et al. 2022) because the sample was not fully saturated (Figs. 9*d* and 10*d*) and the solution/solid ratio was very small, the observed microstructural changes were expected to be related to the acid–base reaction concentrated at particle edges and to the clay mineral dissolution, together with the higher water contents.

Based on the results of this study, modifications concerning the preparation and the installation of the claystone sample as well as the mini-pressure sensor were brought. The findings of this work are of great significance for the understanding of the in situ behavior of the Opalinus Clay exposed to saline and alkaline plumes, which is crucial for the assessment of the long-term safety of the repository.

Article information

History dates

Received: 18 November 2022
Accepted: 6 May 2023
Accepted manuscript online: 24 May 2023
Version of record online: 23 November 2023

Copyright

Data availability

Data generated or analyzed during this study are available from the corresponding author upon reasonable request.

Author information

Author ORCIDs

Nadia Mokni https://orcid.org/0000-0003-1944-9118

Author notes

Yu-Jun Cui served as an Associate Editor at the time of manuscript review and acceptance; peer review and editorial decisions regarding this manuscript were handled by another Editorial Board Member.

Author contributions

Investigation: YB, NM, Y-JC, FB, PD
Supervision: NM, Y-JC, PD, FB
Validation: NM, Y-JC, PD

Competing interests

The authors declare that there are no competing interests.

Funding information

There are no funders to report for this submission.

References

Andra. 1999. Référentiel Géologique du site de l'Est. Andra, Chatenay-Malabry, France, Rapport ADS-99-005.

Andra. 2005. Evaluation of the feasibility of a geological repository in an Argillaceous Formation. Meuse/Haute-Marne site. Andra, Chatenay-Malabry, France, Dossier 2005 Argile.

Barakat, Y., Cui, Y.J., Mokni, N., Delage, P., and Bernier, F. 2022. Effects of pH and exposure time to alkaline solutions on the mineralogy of the Opalinus Clay from the lower sandy facies of Mont Terri site. Engineering Geology, **306**: 106766. doi:10.1016/j.enggeo.2022.106766.

Bossart, P. 2011. Characteristics of the Opalinus clay at Mont Terri. Available from http://www.mont-terri.ch/internet/montterri/fr/home/geology/key_characteristics.parsys.49924.DownloadFile.tmp/characteristicsofopa.pdf.

Bossart, P., and Thury, M. 2008. Mont Terri Rock Laboratory project: programme 1996 to 2007 and results. Swiss Geological Survey, Wabern, Germany.

Brunauer, S., Emmett, P.H., and Teller, E. 1938. Adsorption of gases in multimolecular layers. Journal of the American Chemical Society, **60**(2): 309–319. doi:10.1021/ja01269a023.

Chavali, R.V.P., Vindula, S.K., Reddy, H.P., Babu, A., and Pillai, R. 2017. Swelling behavior of kaolinitic clays contaminated with alkali solutions: a micro-level study. Applied Clay Science, **135**: 575–582. doi:10.1016/j.clay.2016.10.045.

Chen, Y.G., Jia, L.Y., Li, Q., Ye, W.M., Cui, Y.J., and Chen, B. 2017. Swelling deformation of compacted GMZ01 bentonite experiencing chemical cycles of sodium-calcium exchange and salinization-desalinization effect. Applied Clay Science, **141**: 55–63. doi:10.1016/j.clay.2017.02.016.

Chorom, M., and Rengasamy, P. 1995. Dispersion and zeta potential of pure clays as related to net particle charge under varying pH, electrolyte concentration and cation type. European Journal of Soil Science, **46**(4): 657–665. doi:10.1111/j.1365-2389.1995.tb01362.x.

Davy, C.A., Skoczylas, F., Barnichon, J.D., and Lebon, P. 2007. Permeability of macro-cracked argillite under confinement: gas and water testing. Physics and Chemistry of the Earth, Parts A/B/C, **32**(8–14): 667–668. doi:10.1016/j.pce.2006.02.055.

Delage, P., Marcial, D., Cui, Y.J., and Ruiz, X. 2006. Ageing effects in a compacted bentonite: a microstructure approach. Géotechnique, **56**(5): 291–304. doi:10.1680/geot.2006.56.5.291.

Dixon, D., Chandler, N., Graham, J., and Gray, M.N. 2002. Two large-scale sealing tests conducted at Atomic Energy of Canada's underground research laboratory: the buffer-container experiment and the isothermal test. Canadian Geotechnical Journal, **39**(3): 503–518. doi:10.1139/t02-012.

Ferrari, A., Favero, V., and Laloui, L. 2014. Experimental analysis of the retention behavior of shales. International Journal of Rock Mechanics and Mining Sciences, **72**: 61–70. doi:10.1016/j.ijrmms.2014.08.011.

Gaucher, E.C., and Blanc, P. 2006. Cement/clay interactions—a review: experiments, natural analogues, and modeling. Waste Management, **26**(7): 776–788. doi:10.1016/j.wasman.2006.01.027. PMID: 16574392.

Geet, M.V., Bastiaens, W., and Ortiz, L. 2008. Self-sealing capacity of argillaceous rocks: review of laboratory results obtained from the SELFRAC project. Physics and Chemistry of the Earth, Parts A/B/C, **33**: S396–S406. doi:10.1016/j.pce.2008.10.063.

Gonzalez-Blanco, L. 2017. Gas migration in deep argillaceous formations: boom clay and indurated clays. Ph.D. thesis, Universitat politècnica de catalunya Barcelonatech, Barcelona, Spain.

He, Y., Chen, Y.G., Ye, W.M., Chen, B., and Cui, Y.J. 2016. Influence of salt concentration on volume shrinkage and water retention characteristics of compacted GMZ bentonite. Environmental Earth Science, **75**: 535. doi:10.1007/s12665-015-5228-3.

Kneuker, T., and Furche., M. 2021. Capturing the structural and compositional variability of Opalinus Clay: constraints from multidisciplinary investigations of Mont Terri drill cores (Switzerland). Environmental Earth Science, **80**: 421. doi:10.1007/s12665-021-09708-1.

Lalan, P. 2016. Influence d'une température de 70 °C sur la géochimie, la microstructure et la diffusion aux interfaces béton/argile: expérimentations en laboratoire, in situ et modélisation. Ph.D. thesis, PSL Research University, Paris, France.

Lauper, B., Jaeggi, D., Deplazes, G., and Foubert, A. 2018. Multi-proxy facies analysis of the Opalinus Clay and depositional implications (Mont Terri rock laboratory, Switzerland). Swiss Journal of Geosciences, **111**: 383–398. doi:10.1007/s00015-018-0303-x.

Lerouge. 2014. Collaborative work between BRGM and University of Bern, unpublished.

Matray, J.M., and Möri, A. 2012. Petrophysical measurements on BCD-3 core samples from the Mont Terri rock laboratory. IRSN, Fontenay-aux-Roses, France, Note technique IRSN/PRP- DGE/2012-00020.

Matray, J.M., Savoye, S., and Cabrera, J., 2007. Desaturation and structure relationships around drifts excavated in the well-compacted Tournemire's argillite (Aveyron, France). Engineering Geology, **90**(1–2): 1–16. doi:10.1016/j.enggeo.2006.09.021.

Menaceur, H., Delage, P., Tang, A.M., and Conil, N. 2016. On the thermo-hydro-mechanical behaviour of a sheared Callovo-Oxfordian claystone sample with respect to the EDZ behaviour. Rock Mechanics and Rock Engineering, **49**(5): 1875–1888. doi:10.1007/s00603-015-0897-5.

Mitchell, J.K. 1993. Fundamentals of soil behavior. 2nd ed. Wiley, New York, NY.

Mokni, N. 2011. Deformation and flow induced by osmotic processes in porous materials. Ph.D. thesis, Technical University of Catalunya, Barcelona, Spain.

Monfared, M., Sulem, J., Delage, P., and Mohajerani, M. 2014. Temperature and damage impact on the permeability of Opalinus Clay. Rock Mechanics and Rock Engineering, **47**: 101–110. doi:10.1007/s00603-013-0459-7.

Monnier, G., Stengel, P., and Fies, J.C. 1973. Une méthode de mesure de la densité apparente de petits agglomérats terreux. Application à l'analyse de système de porosité du sol. Annales Agronomiques, **24**(5): 533–545.

Nagra. 2002. Synthese der Geowissenschaftlichen Unter-suchungserge bnisse. Nagra, Baden, Switzerland, Technischer Bericht 02-03.

Ould Bouya, M.L. 2014. Acquisition d'un profil de perméabilité intrinsèque au sein de l'Argile à Opalines du Mont Terri par analyse minéralogique et pétrophysique. Mémoire de Master, Université Paris-Sud 11, Orsay, France.

Pearson, F.J., Arcos, D., Boisson, J.Y., Fernández, A.M., Gäbler, H.E., Gaucher, E., et al. 2003. Mont Terri Project: geochemistry of water in the Opalinus Clay Formation at the Mont Terri Rock Laboratory. Reports of the FOWG, Bern, Switzerland, Geology Series, No. 5.

Pedrotti, M., and Tarantino, A. 2018. An experimental investigation into the micromechanics of non-active clays. Géotechnique, **68**(8): 666–683. doi:10.1680/jgeot.16.P.245.

Sing, K.S.W. 1991. Characterization of porous solids: an introductory survey. Studies in Surface Science and Catalysis, **62**: 1–9. doi:10.1016/S0167-2991(08)61303-8.

Sun, W.J., and Cui, Y.J. 2020. Determining the soil-water retention curve using mercury intrusion porosimetry test in consideration of soil volume change. Journal of Rock Mechanics and Geotechnical Engineering, **12**(5): 1070–1079. doi:10.1016/j.jrmge.2019.12.022.

Taylor, H.F.W. 1987. A method for predicting alkaline concentrations in cement pore solutions. Advances in Cement Research, **1**(1): 5–17. doi:10.1680/adcr.1987.1.1.5.

Thyagaraj, T., and Rao, S.M. 2013. Osmotic swelling and osmotic consolidation behaviour of compacted expansive clay. Geotechnical and Geological Engineering, **31**(2): 435–445. doi:10.1007/s10706-012-9596-0.

Wahid, A.S., Gajo, A., and Di Maggio, R. 2011a. Chemo-mechanical effects in kaolinite. Part 1: prepared samples. Géotechnique, **61**(6): 439–447. doi:10.1680/geot.8.P.067.

Wahid, A.S., Gajo, A., and Di Maggio, R. 2011b. Chemo-mechanical effects in kaolinite. Part 2: exposed samples and chemical and phase analyses. Géotechnique, **61**(6): 449–457. doi:10.1680/geot.8.P.068.

Wilson, M.J., Wilson, L., and Patey, I. 2014. The influence of individual clay minerals on formation damage of reservoir sandstones: a critical review with some new insights. Clay Minerals, **49**(2): 147–164. doi:10.1180/claymin.2014.049.2.02.

Ye, W.M., Zheng, Z.J., Chen, B., Chen, Y.G., Cui, Y.J., and Wang, J. 2014. Effects of pH and temperature on the swelling pressure and hydraulic conductivity of compacted GMZ01 bentonite. Applied Clay Science, **101**(1): 192–198. doi:10.1016/j.clay.2014.08.002.

Ye, W.M., Zhu, C.M., Chen, Y.G., Chen, B., Cui, Y.J., and Wang, J. 2015. Influence of salt solutions on the swelling of the compacted GMZ01 bentonite. Environmental Earth Science, **74**: 793–802. doi:10.1007/s12665-015-4108-1.

Yu, C. 2017. Comparative study of convective and diffusive transport phenomena within the Opalinus clay of Mont Terri. Ph.D. thesis, Aix Marseille université, Marseille, France.

Zhang, C. 2011. Experimental evidence for self-sealing of fractures in claystone. Physics and Chemistry of the Earth, Parts A/B/C, **36**(17–18): 1972–1980. doi:10.1016/j.pce.2011.07.030.

Zhang, C. 2013. Sealing of fractures in claystones. Journal of Rock Mechanics and Geotechnical Engineering, **5**(3): 214–220. doi:10.1016/j.jrmge.2013.04.001.

Zhang, C. 2016. The stress-strain-permeability behavior of clay rock during damage and recompaction. Journal of Rock Mechanics and Geotechnical Engineering, **8**(1): 16–26. doi:10.1016/j.jrmge.2015.10.001.

Zhang, C., and Rothfuchs, T. 2008. Damage and sealing of clay rocks detected by measurements of gas permeability. Physics and Chemistry of the Earth, Parts A/B/C, **33**: S363–S373. doi:10.1016/j.pce.2008.10.013.

Zhu, C.M., Ye, W.M., Chen, Y.G., Chen, B., and Cui, Y.J. 2013. Influence of salt solutions on the swelling pressure and hydraulic conductivity of compacted GMZ01 bentonite. Engineering Geology, **166**: 74–80. doi:10.1016/j.enggeo.2013.09.001.